CrossMark

A Novel Asymmetric Supercapacitor Designed with Mn$_3$O$_4$@Multi-wall Carbon Nanotube Nanocomposite and Reduced Graphene Oxide Electrodes

MANAS MANDAL,[1] DEBASIS GHOSH,[1] KRISHNA CHATTOPADHYAY,[2] and CHAPAL KUMAR DAS[1,3]

1.—Materials Science Centre, Indian Institute of Technology Kharagpur, Kharagpur 721302, India. 2.—Department of Chemistry, Indian Institute of Technology Kharagpur, Kharagpur 721302, India. 3.—e-mail: chapal12@yahoo.co.in

We demonstrate a straightforward process for the synthesis and fabrication of a hybrid-type asymmetric supercapacitor (ASC) by combining Mn$_3$O$_4$ nanoparticle-supported multi-wall carbon nanotube (Mn$_3$O$_4$@MWCNT) composite as positive and reduced graphene oxide (rGO) as negative electrodes. A controlled hydrothermal synthesis of Mn$_3$O$_4$ in the presence of MWCNT resulted in a well-distributed Mn$_3$O$_4$ nanoparticles on the MWCNT backbone in the Mn$_3$O$_4$@MWCNT composite. The structure and morphology of the as-prepared materials have been investigated by x-ray diffraction, Fourier transform infrared spectroscopy, field-emission scanning electron microscopy, transmission electron microscopy, Brunauer–Emmett–Teller analysis and x-ray photoelectron spectroscopy measurements. The electrochemical characterizations were carried out in terms of cyclic voltammetry, galvanostatic charge–discharge (GCD) and electrochemical impedance spectroscopy analysis. The constructed ASC with 1 M KOH-supporting electrolyte was able to provide high-specificity capacitance of 173.36 F/g at 2 mV/s scan rate and high-energy density of 26.8 Wh/kg accompanied by high cycle stability with 79.3% capacitance retention over 3000 GCD cycles.

Key words: Asymmetric supercapacitor, composites, Mn$_3$O$_4$, reduced graphene oxide, pseudocapacitance

INTRODUCTION

A sustainable and renewable energy resource is required as an alternative to the world's growing energy needs without causing any environmental detriment.[1] Solar energy and wind energy as renewable sources have attracted global attention, but these are unreliable energy sources due to their uncertain and intermittent behavior.[2] Recently, electrochemical capacitors, also known as supercapacitors (SCs), have drawn tremendous attention with their great potential application in the field of energy storage due to their unique properties of high power density, long cycle life, low maintenance cost and green environmental protection.[3,4]

Although SCs deliver very high power density ($\sim$10 W/kg to 10^4 W/kg), they suffer from lower energy density ($\sim$0.2 Wh/kg to 10 Wh/kg) compared to conventional batteries ($\sim$10 Wh/kg to 200 Wh/kg).[5] The energy density (E) is related to the operating voltage (V) and capacitance according to the following equation: $E = 0.5CV^2$. To achieve high energy density along with high power density and long cycle life, efforts have been devoted to developing asymmetric supercapacitors (ASCs) by combining a battery-like Faradaic electrode (as energy source) and a capacitive electrode (as power source).[6] So far, various redox active metal oxides or hydroxides, such as Mn$_3$O$_4$,[7,8] Fe$_3$O$_4$,[9] Co$_3$O$_4$, Co(OH)$_2$,[10] Ni(OH)$_2$[11,12] and their composites with

carbonaceous materials graphene or/and carbon nanotubes, have been investigated as supercapacitor active material. Amongst these, Mn_3O_4 can be considered as one of the most promising electrode materials because of its low cost and environmental compatibility accompanied by high pseudocapacitance.[13] However, the poor electrical conductivity often results in low rate capability in these metal oxides. In this context, an increase in electrical conductivity of the pseudocapacitive metal oxides in terms of nanocomposites with other carbonaceous materials would be helpful, as they are highly conductive in nature.

Recently, activated carbon (AC) has been extensively used for the capacitive electrodes of ASCs due to its high specific surface area and moderate cost. However, it suffers from small pore diameter (0.5 nm), which is not accessible to hydrate ions (0.6–0.76 nm) resulting in a poor capacitive performance.[14,15] In order to minimize this problem, reduced graphene oxide (rGO) nanosheet has been employed instead of AC. Recently, rGO has attracted extensive attention in energy research due to its unique properties, such as a flexible porous structure with mesopores and microspores, high surface area, high conductivity, high energy density, good electrochemical stability, etc.[6,11,16]

Here, we have reported a simple hydrothermal method for the synthesis of Mn_3O_4/multi-wall carbon nanotube (Mn_3O_4@MWCNT) nanocomposite as a supercapacitor electrode material with improved rate capability. To obtain an improved cell voltage in an aqueous electrolyte, an aqueous ASC has been constructed by combining Mn_3O_4@MWCNT and rGO as positive and negative electrodes, respectively, which was able to show a high cell voltage of 1.6 V resulting in high energy density of 26.8 Wh/kg.

EXPERIMENTAL

Preparation of Pure Mn_3O_4 and Mn_3O_4@MWCNT Composite

A simple and cost-effective hydrothermal method was carried out for the synthesis of Mn_3O_4 by using $MnCl_2 \cdot 4H_2O$ as metal precursor and ethanolamine (EA) as hydrolysing agent. For the synthesis of the Mn_3O_4@MWCNT composite, a hydrothermal reaction was carried out in the presence of dispersed MWCNTs in water. Briefly, 30 mg MWCNTs was dispersed in 20 mL water by ultrasonication for 45 min and was mixed with 20 mL 0.1 M aqueous solution of $MnCl_2 \cdot 4H_2O$. Then, the whole mixture was again ultrasonicated for 15 min followed by drop-by-drop addition of ethanolamine (0.4 mL) into the solution mixture under vigorous stirring condition. The whole solution mixture was transferred into a 50-mL autoclave and kept in a muffle furnace for 6 h at 180°C. The greenish-black precipitate was washed with a water and ethanol mixture five times and dried at 70°C. The pure Mn_3O_4 was prepared by

following the same procedure without the addition of MWCNT.

Preparation of rGO

Reduced graphene oxide was prepared by the hydrothermal reduction of graphene oxide in presence of L-ascorbic acid. Graphene oxide (GO) was prepared by a modified Hummers' method.[17] Briefly, 1 g of commercially available fine graphite powder was dispersed in a mixture of concentrated H_2SO_4 (120 mL) and ortho-phosphoric acid (13.3 mL). Then, 6 g $KMnO_4$ was added pinch-by-pinch to avoid excess heating. After 12 h stirring, the whole mixture was poured slowly into a mixture of 30% H_2O_2 (1.5 mL) in ice water. The GO powder was collected after washing the solid material successively with 10% HCl, water and ethanol. Reduced graphene oxide was prepared by the reduction of the as-prepared GO with ascorbic acid. 50 mg GO with 50 mg L-ascorbic acid was ultrasonicated in 40 mL H_2O for 30 min. Then, the mixture solution was transferred into a 50-mL Teflon autoclave and kept in a muffle furnace at 180°C for 6 h. The product was washed with a water and ethanol mixture and dried at 60°C.

RESULTS AND DISCUSSION

Ethanolamine (EA), an organic solvent, has been extensively used for the synthesis of a variety of types of nanostructured metal oxides such as Mn_3O_4,[8] Fe_3O_4,[18] Co_3O_4,[19] SnO,[20] etc. as a hydrolyzing agent. The schematic presentation of the formation of the Mn_3O_4@MWCNT composite is shown in Scheme 1. Mn_3O_4 nanoparticles were formed via a Mn–EA complex formation (Scheme 1b).[21] Similarly, the composite with MWCNT followed the same mechanism where the MWCNT served as a template.
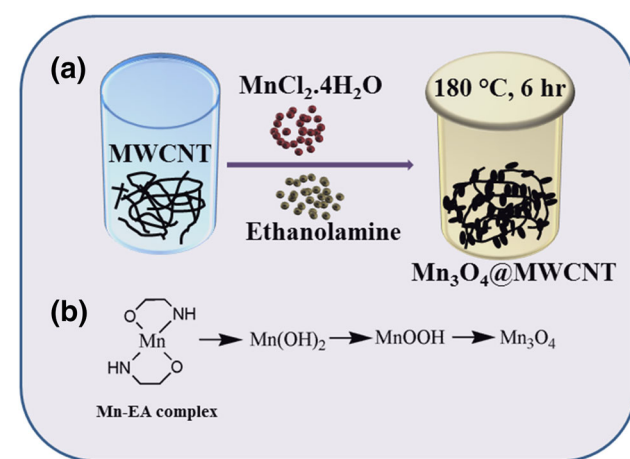
Scheme 1. The schematic diagram of the synthesis of composite (a); the mechanism of the formation of Mn_3O_4 nanoparticles (b).

A Novel Asymmetric Supercapacitor Designed with Mn_3O_4@Multi-wall Carbon Nanotube Nanocomposite and Reduced Graphene Oxide Electrodes

3493

The as-prepared materials were characterized by x-ray diffraction (XRD) analysis, Fourier transform infrared (FTIR) spectroscopy, Raman spectroscopy study, x-ray photoelectron spectroscopy (XPS), field-emission scanning electron microscopy (FESEM) and transmission electron microscopy (TEM) for structural, chemical composition and morphological determination. The surface area of the material was determined by the N_2 adsorption–desorption isotherm. The electrochemical behavior was analyzed in terms of cyclic voltammetry (CV), galvanostatic charge–discharge (GCD) curve and electrochemical impedance spectra (EIS).

XRD Analysis

The XRD analysis was carried out using a Rigaku ULTIMA-III x-ray diffractometer with Cu Kα radiation (λ = 1.548 Å). The XRD pattern of Mn_3O_4 and the Mn_3O_4@MWCNT composite is shown in Fig. 1a. The diffraction pattern of Mn_3O_4 is well matched with the JCPDS card no. 04-007-1841. The peaks at 2θ = 18.01, 28.91, 30.99, 32.38, 36.08, 38.09, 44.40, 49.89, 53.86, 56.02, 59.9 and 64.61 degrees correspond to the planes of (101), (112), (200), (103), (211), (004), (220), (204), (312), (303), (224) and (314), respectively. All these peaks are also present in the Mn_3O_4@MWCNT composite with an additional peak at 2θ = 26°, which can be attributed to the (002) plane of MWCNT.[22] Figure S1a (see supplementary materials) shows the XRD pattern of GO and rGO. For GO, the characteristics peak of the (002) plane of GO arises at 2θ = 10.2° which is missing in rGO, indicating the successful reduction of GO.

FTIR Analysis

The chemical compositions of the as-prepared materials were also confirmed by FTIR analyses, which are shown in Fig. 1b. For this characterization, a disc-shaped pellet was first prepared from as-prepared powder samples and then the analysis was done using a NEXUS 870 FTIR (Thermo Nicolet) instrument. The stretching frequencies at 615 cm^{-1} and 500 cm^{-1} indicate the stretching modes of tetrahedral and octahedral sites of Mn_3O_4.[23,24] The peak at 3405 cm^{-1} is attributed to the presence of physisorbed water molecules in the materials. The –C=C– stretching frequency of MWCNT arises at 1564 cm^{-1} in the composite spectrum along with other peaks of Mn_3O_4.[25] Figure S1b (see supplementary materials) shows the FTIR spectra of GO and rGO. The obtained peaks for GO are well-matched with the literature. The peaks at 1726 cm^{-1}, 1623 cm^{-1}, 1400 cm^{-1}, 1232 cm^{-1} and 1049 cm^{-1} are attributed to C=O (carboxyl/carbonyl), C=C (aromatic), C–O (carboxy), C–O (epoxy) and C–O (alkoxy), respectively.[26–28] In the case of rGO, almost all the peaks were diminished, indicating successful reduction to a large degree.

Raman Study

Raman spectroscopy also confirmed the successful formation of the Mn_3O_4@MWCNT composite which was carried out at an excitation wave length of 488 nm. The bands (Fig. 2) observed at 289 cm^{-1}, 316 cm^{-1}, 372 cm^{-1}, 478 cm^{-1}, and 657 cm^{-1} confirm the crystalline Mn_3O_4 nanoparticles in the composite.[29,30] The most intense peak at 657 cm^{-1} can be considered as the characteristic peak for spinel Mn_3O_4 having A_g symmetry, which appears due to the interior movement of oxygen in the octahedral unit, MnO_6. The peaks at 1334 cm^{-1} and 1599 cm^{-1} can be attributed to the D and G bands of MWCNT.[31,32] The D band mainly originates from the structural defects on the surface of MWCNT and the G band stands for the E_{2g} graphite mode.
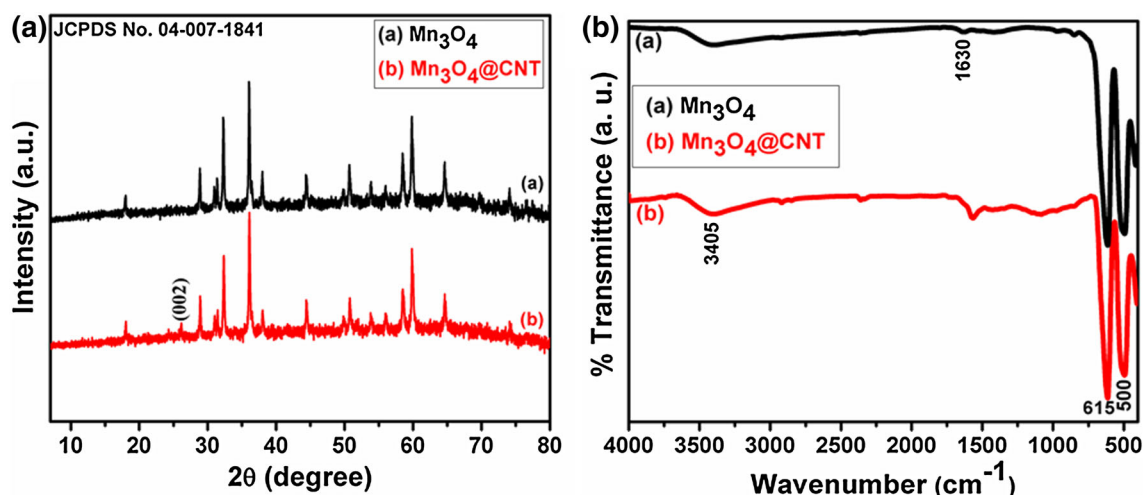

Fig. 1. XRD pattern (a) and FTIR spectra (b) of pure Mn_3O_4 and the Mn_3O_4@MWCNT composite.
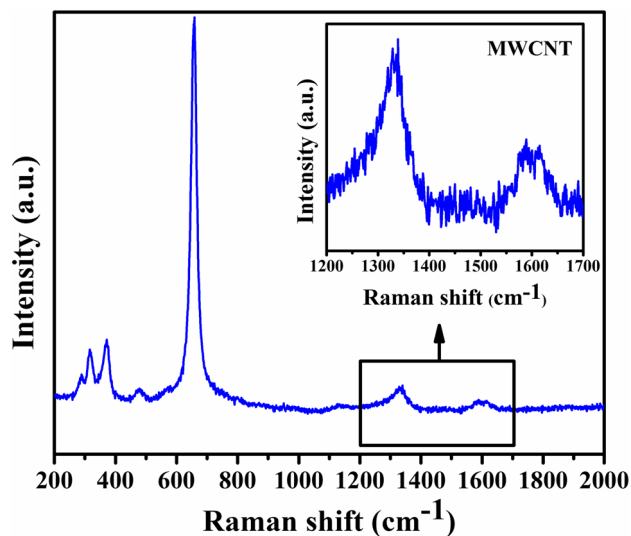
Fig. 2. Raman spectrum of the as-prepared Mn_3O_4-MWCNT composite; inset the enlarged peaks for MWCNT.
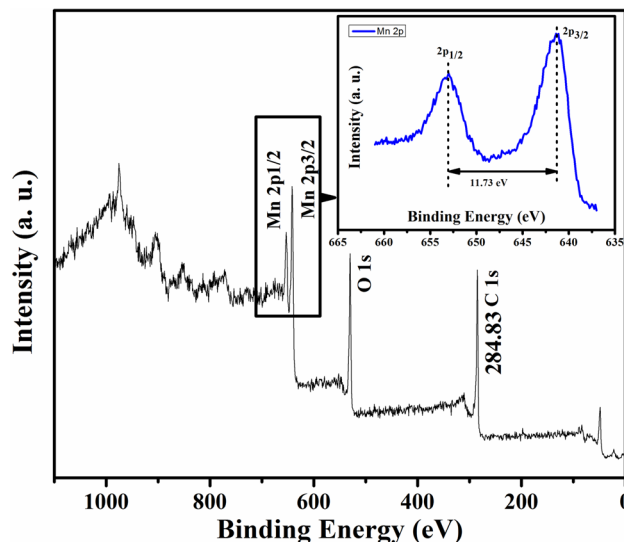

Fig. 3. XPS spectrum (survey scan) of the Mn_3O_4-MWCNT composite; inset magnified view of Mn2p level.

XPS Study

For the chemical analysis of the composite, XPS was carried out using a PHI 5000 Versa Probe II XPS analyzer with a monochromatic Al Kα x-ray source ($h\upsilon$ = 1486.71 eV). Figure 3 shows the survey scan of XPS spectra for the Mn_3O_4@MWCNT composite where all the peaks of C, Mn and O can be seen. The C 1s peak at the binding energy of 284.83 eV indicates the presence of MWCNTs in the composite.[33] The Mn2p level spectrum is shown in the inset of Fig. 3. For Mn2p, the two peaks at 653.0 eV and 641.27 eV are attributed to Mn2p1/2 and Mn2p3/2, respectively, with the spin energy difference of 11.73 eV, confirming the Mn_3O_4 formation.[34]

Morphological Analysis

The morphological analysis of the as-prepared Mn_3O_4, Mn_3O_4@MWCNT and rGO were carried out in terms of FESEM and TEM analyses using a Carl Zeiss-SUPRA 40 and a TECNAI G2-20S-TWIN, respectively. Figure 4a shows the FESEM image of Mn_3O_4 nanoparticles with an average dimension of tens of nanometers. The corresponding TEM image of the pure Mn_3O_4 nanoparticles are represented in Fig. 4b, supporting the FESEM observation. In case of the Mn_3O_4@MWCNT composite, the MWCNTs backbone served as the template to grow the Mn_3O_4 nanoparticles (Fig. 4c). This is also confirmed from the TEM analysis (Fig. 4d), in which, apart from just a few agglomerated nanoparticles, Mn_3O_4 nanoparticles were nicely distributed. Here, MWCNT acted both as a template for the growth of Mn_3O_4 nanoparticles as well connecting individual nanoparticles and, thereby, a conductive network was formed inside the composite. Energy dispersive x-ray spectroscopy (EDX) analyses of

Mn_3O_4 and Mn_3O_4@MWCNT are shown in Fig. 4e and f, respectively. Fig. S2a (see supplementary materials) shows that the as-prepared reduced graphene oxide merely formed a network-like morphology which is clearly seen from the corresponding TEM images (Fig. S2b) (see supplementary materials).

Brunauer–Emmett–Teller (BET) Analysis

The effective BET surface area of the composite was calculated using a Quantachrome Chem BET analyzer, as the surface area of an electrode material plays a crucial role in determining its performance. The composites show a high surface area and porosity obtained from the N_2 adsorption–desorption isotherm and Barrett–Joyner–Halenda (BJH) methods, and the plots are shown in Fig. 5. According to the International Union of Pure and Applied Chemistry, the BET isotherm exhibits a type-4 isotherm with H3 hystorysis loop. The BET surface area of the composite was found to be 64.68 m^2/g. The BJH pore size distribution profile (Fig. 5, inset) shows perfectly monomodal distribution with the maxima of 17.1 nm for the composite. The surface area of the rGO was determined to be 95.92 m^2/g (Fig. S3) (see supplementary materials).

Electrochemical Characterizations

The electrochemical properties of Mn_3O_4, Mn_3O_4@MWCNT, and rGO were studied in a three-electrode cell where the active materials, coated Ni foam, Pt foil and saturated calomel electrode, (SCE) were used as the working electrode, counter electrode and reference electrode, respectively, in 1 M KOH electrolyte using a Biologic SP-150 instrument. For the preparation of the working electrode, cleaned Ni foam (1 × 1 cm) was taken as
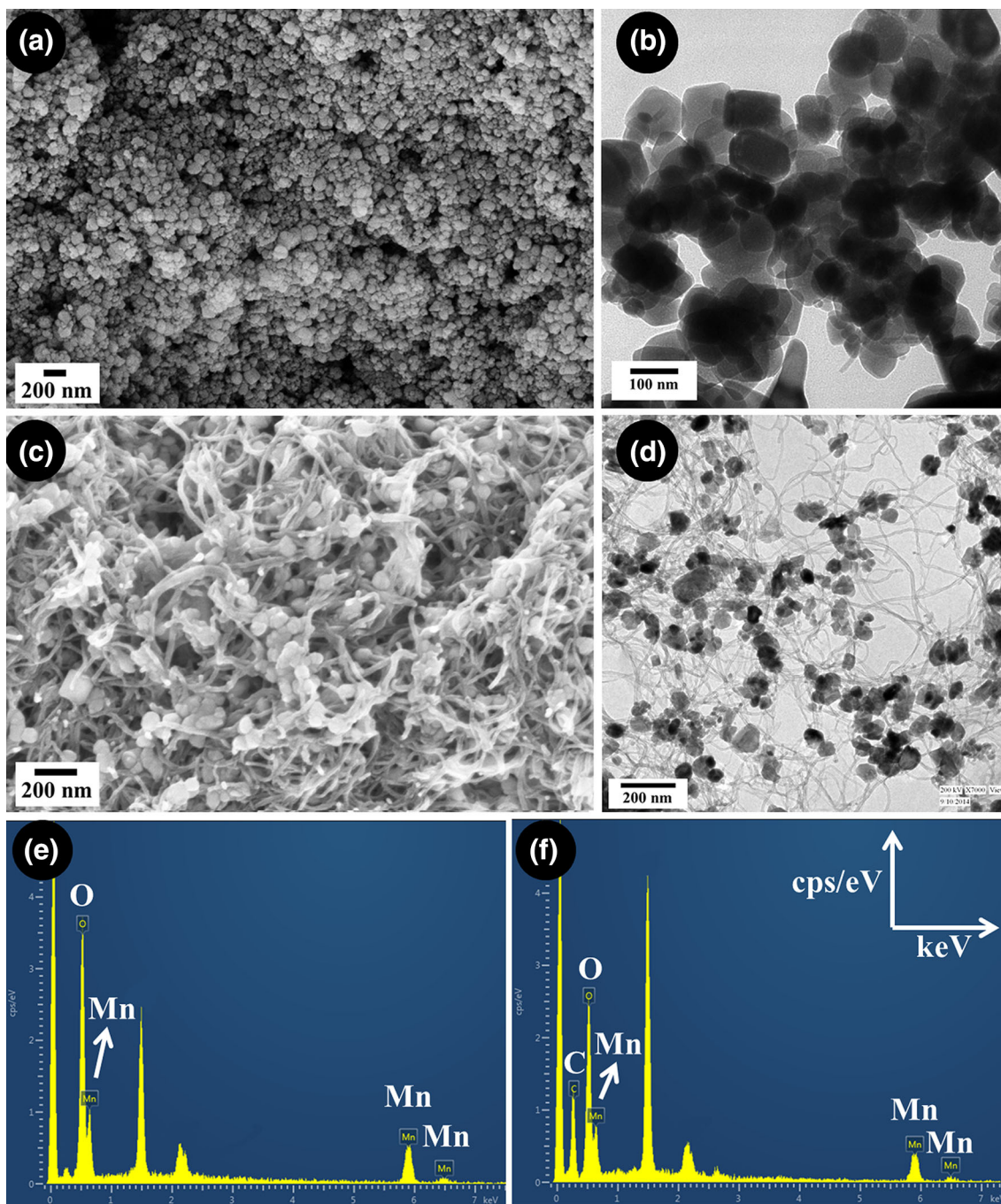
Fig. 4. FESEM images of the as-prepared Mn_3O_4 (a), Mn_3O_4@MWCNT (c); TEM images of Mn_3O_4 (b), Mn_3O_4@MWCNT (d); EDAX spectra of Mn_3O_4 (e), Mn_3O_4@MWCNT (f).

the current collector on which active materials paste was cast. The Ni foam was cleaned via ultrasonication for 30 min in 30% HCl to remove the NiO layer on the surface. The active material paste was prepared by mixing it with carbon black (to increase the conductivity) and polyvinylidene fluoride (as binder) with 8:1:1 weight ratio in N-methyl-2-pyrrolidone (NMP) solvent. The as-prepared paste was cast onto the cleaned Ni foam and dried under air.

Electrochemical characterization techniques in terms of cyclic voltammetry (CV), galvanostatic charge–discharge (GCD) and electrochemical impedance spectroscopy (EIS) were employed for the as-prepared electrode materials. The CV plots of the Mn_3O_4 and Mn_3O_4@MWCNT at different scan rates of 2 mV/s, 5 mV/s, 10 mV/s, 20 mV/s, 50 mV/s and 100 mV/s are shown in Fig. 6a and b, respectively, with a potential window of 0 V to 0.6 V (versus SCE). A pair of redox peaks appeared for both the
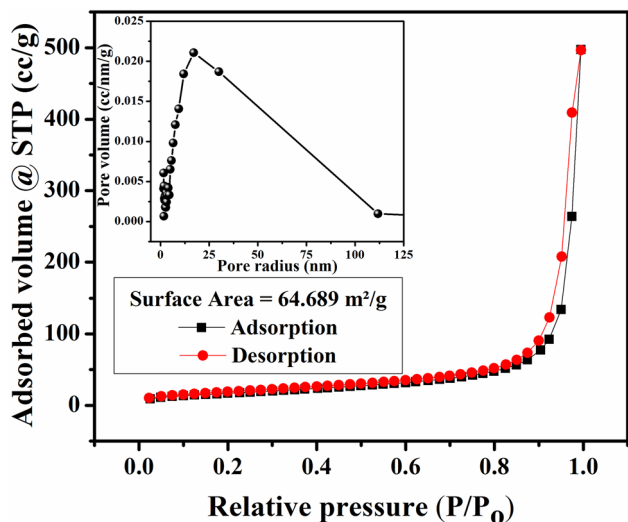
Fig. 5. N_2 adsorption–desorption isotherms and BJH pore size distribution profile (inset) of Mn_3O_4@MWCNT composite.

electrode materials, indicating the occurrence of a Faradaic redox reaction during the CV cycle in the KOH electrolyte. The redox peak positions in the CV plot clearly indicate the reversible redox reaction of Mn(III)/Mn(II), Mn(IV)/Mn(III) and Mn(VI)/Mn(IV) of Mn_3O_4.[35] The associated redox phenomenon of Mn_3O_4 in an aqueous electrolyte can be expressed as[36]:

$$MnO_x(OH)_y + \delta H_2O + \delta e^- \leftrightarrow MnO_{x-\delta}(OH)_{y+\delta} + \delta OH^- \tag{1}$$
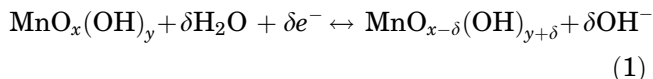
The two oxymanganese species, $MnO_x(OH)_y$ and $MnO_{x-\delta}(OH)_{y+\delta}$, in Eq. 1 are at higher and lower oxidation states, respectively. However, a certain resistive phenomenon was observed as indicated by the positive and negative shifting of the respective anodic and cathodic peaks in the CV plot with the increasing scan rate. The non-rectangular nature of
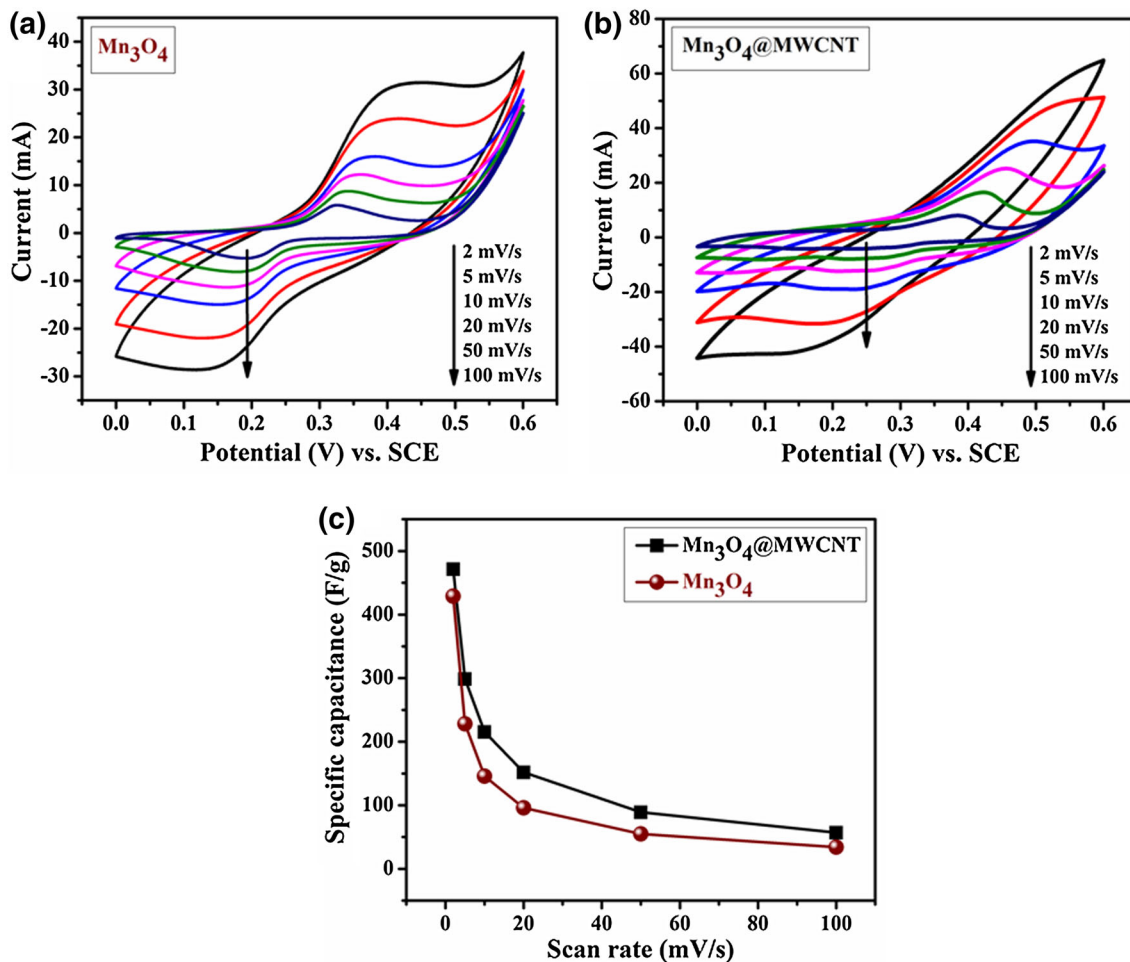

Fig. 6. CV curves of Mn_3O_4 (a) and Mn_3O_4@MWCNT (b) at different scan rates of 2 mV/s, 5 mV/s, 10 mV/s, 20 mV/s, 50 mV/s and 100 mV/s; variation of specific capacitance of Mn_3O_4 and Mn_3O_4@MWCNT at various scan rates (c).
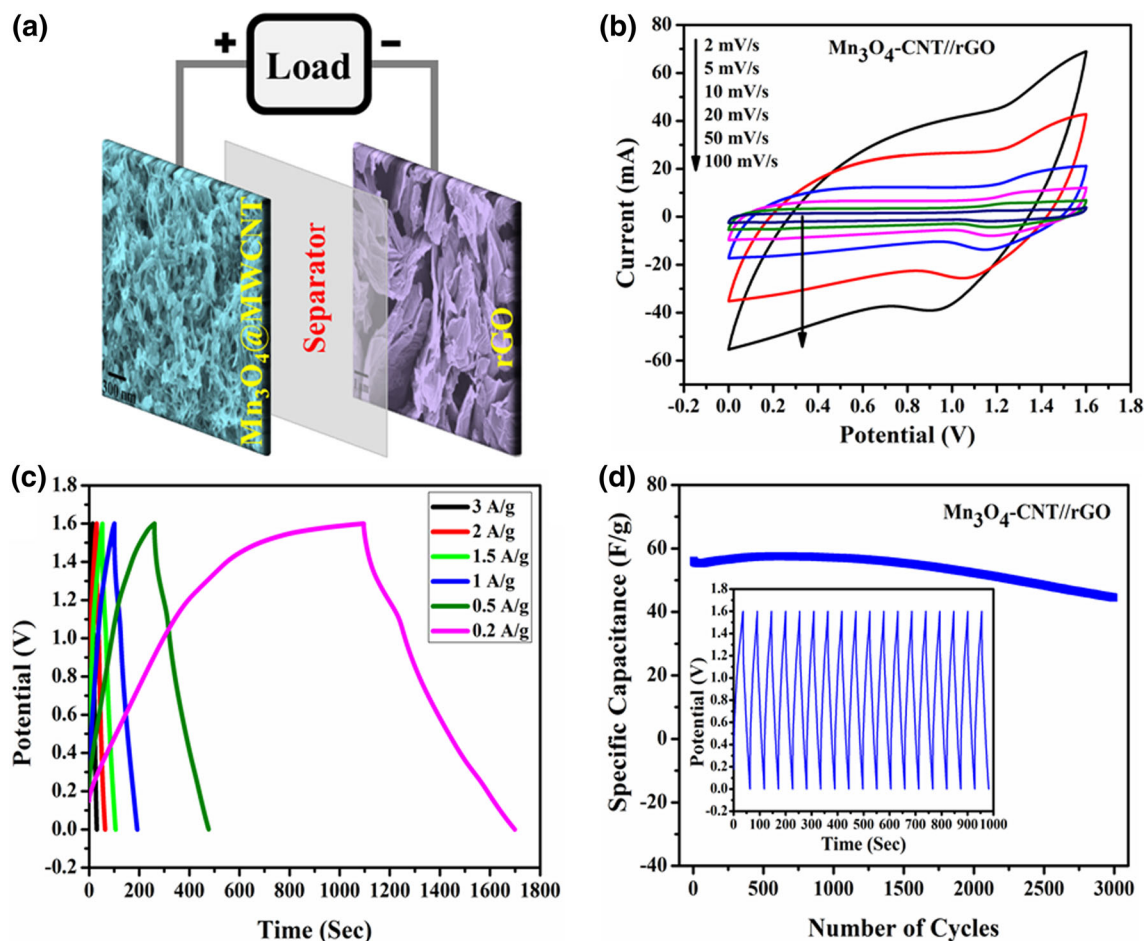
Fig. 7. Schematic of the as-constructed asymmetric supercapacitor by combining Mn_3O_4@MWCNT and rGO as positive and negative electrodes, respectively (a); CV curves of Mn_3O_4@MWCNT//rGO at different scan rates of 2 mV/s, 5 mV/s, 10 mV/s, 20 mV/s, 50 mV/s and 100 mV/s (b); GCD curves of Mn_3O_4@MWCNT//rGO with a cell voltage of 1.6 V at a current varying from 0.2 A/g to 3 A/g (c); cycling performance of Mn_3O_4@MWCNT//rGO at a current of 3 A/g (d).

Table I. Calculated specific capacitance (F/g) of Mn_3O_4@MWCNT//rGO at different scan rates

Scan rate (mV/s)	2	5	10	20	50	100
Specific capacitance (F/g)	173.4	154	139.2	122.3	95.1	71.5

the CV plots also suggests the pseudocapacitive behavior of the active material. However, the CV plots of rGO (Fig. S4; see supplementary materials) showed close to rectangular shape indicating its double-layer capacitive behavior; the soft deviation from a perfect rectangular nature may be due to the residual surface functional group, which in fact contributes some pseudocapacitance to the total capacitance. The specific capacitance from the CV plot was calculated using Eq. 2:

$$\text{Specific capacitance}, C_s = \frac{\int_{V2}^{V1} i(V)dV}{(V2 - V1)vm} \quad (2)$$

where, $\int_{V2}^{V1} i(V)dV$ is the area of the CV curve, $(V2 - V1)$ is the potential window (V), v is the scan rate (mV/s) and m is the mass (g) of the active materials. The highest specific capacitances of 428.9 F/g and 471.3 F/g were achieved for Mn_3O_4 and Mn_3O_4@MWCNT, respectively, at a scan rate of 2 mV/s. For reduced graphene oxide, the obtained maximum specific capacitance was 291 F/g at a scan rate of 2 mV/s with a potential range of 0 V to −1.0 V (vs. SCE). The specific capacitances of the pure Mn_3O_4 and Mn_3O_4@MWCNT composites at various scan rates are shown in Fig. 6c.
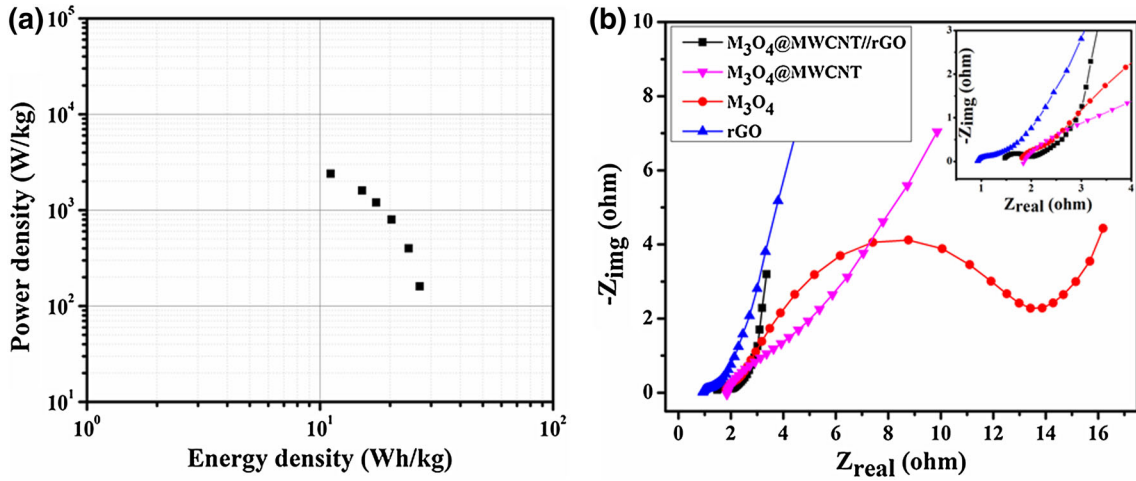
Fig. 8. Ragone plot of Mn_3O_4@MWCNT//rGO in terms of power density versus energy density (a). Nyquist plots of Mn_3O_4, Mn_3O_4@MWCNT, rGO, and Mn_3O_4@MWCNT//rGO (b).

Table II. R_s and R_{ct} values obtained from the fitted plot

Equivalent circuit: $R_s + Q/(R_{ct} + W)$	Mn_3O_4	Mn_3O_4@MWCNT	rGO	Mn_3O_4@MWCNT//rGO
R_s	1.924	1.832	0.914	1.402
R_{ct}	12.7	2.278	0.322	1.211

With the increasing scan rate, the fast voltage alternation results in a low diffusion of electrolyte ions inside the active material, which affects the capacitance. However, the specific capacitance of the composite is always higher than the pure Mn_3O_4 at each scan rate. This is mainly because of the synergistic effect between the high surface area and the highly conductive MWCNT and redox active Mn_3O_4.

An ASC was constructed by combining the Mn_3O_4@MWCNT nanocomposite and rGO nanosheets as positive and negative electrodes, respectively. The schematic illustration of as-constructed ASC shown in Fig. 7a. In order to get the maximum performance in the ASCs, there should be a charge balance between the positive and negative electrodes following Eq. 3:

$$C_+ * V_+ * m_+ = C_- * V_- * m_- \qquad (3)$$

where C is the specific capacitance, V is the potential window, and m is the mass of corresponding electrode. From Eq. 3, the optimum mass ratio of the positive and negative electrodes was found to be unity. Considering the effective working potential of the individual electrodes, measured in a three-electrode system, the initial working potential was chosen as 0–1.6 V for the ASC.

Figure 7b indicates the typical CV curves of Mn_3O_4@MWCNT//rGO at different scan rates of 2–100 mV/s in a 1 M KOH electrolyte within the potential range of 0–1.6 V. The various specific

capacitances obtained at different scan rates are shown in Table I. The maximum specific capacitance obtained for the ASC was 173.4 F/g achieved at a scan rate of 2 mV/s. On increasing the scan rates, the specific capacitance decreased, with a still high capacitance retention of 71.5 F/g at the high scan rate of 100 mV/s, which indicates an excellent rate capability of the as-fabricated supercapacitor. The GCD curves of Mn_3O_4@MWCNT//rGO at different currents from 0.2 A/g to 3 A/g in 1 M KOH aqueous electrolyte are shown in Fig. 7c. The nature of the GCD curves indicates the involvement of pseudocapacitance in the total capacitance. The specific capacitance from the GCD curves was calculated from Eq. 4:

$$\text{Specific capacitance}, C_S = \frac{i \times \Delta t}{m \times \Delta v} \qquad (4)$$

where, i is the applied current, Δt is the discharge time, m is the mass of active material, and Δv is the potential window. The calculated specific capacitances of the constructed ASC are 75.4 F/g, 67.5 F/g, 57 F/g, 49 F/g, 42.7 F/g and 31.3 F/g at the currents of 0.2 A/g, 0.5 A/g, 1 A/g, 1.5 A/g, 2 A/g and 3 A/g, respectively. The achieved specific capacitance is higher than the Mn_3O_4@GR//AC ASC which showed 38 F/g and 62 F/g at 0.5 A/g in 6 M KOH and 1 M Na_2SO_4 electrolyte, respectively.[8] It can be seen that the capacitance gradually decreases with the increase of the current. This is mainly due to the limiting diffusion of electrolytes ion at higher

currents; hence, only the outer surface is used for effective charge storage. Although the performance of the as-fabricated ASC is appraisable, there remains a performance reduction regarding the low columbic efficiency. In order to increase the columbic efficiency, the electrochemical tests were repeated within the potential range of 0–1.4 V. The electrochemical analyses are presented in Fig. S5 in the supplementary materials.

Figure 7d shows the standard cyclic stability with 79.3% specific capacitance retention over 3000 consecutive GCD cycles at 1 A/g current within the potential range 0–1.6 V. Interestingly, within the potential range of 0–1.4 V, the ASC showed high capacitance retention of 76% after 10,000 consecutive GCD cycles at a three times higher current density (Fig. S5c, supplementary materials). This may be due to some sort of irreversible reaction beyond that potential range, that causes a greater extent of capacitance decay. The energy density and power density are the main two parameters that play key roles in determining the performance of the supercapacitor. The energy density and power density were measured by Eqs. 5 and 6, respectively:

$$\text{Energy density, } E = \frac{1}{2 \times 3.6} C_s (\Delta V)^2 \qquad (5)$$

$$\text{Power density, } P = \frac{E}{T} \times 3600 \qquad (6)$$

where C_s is the specific capacitance, ΔV is the potential window and T is the discharging time. The maximum energy density of 26.816 Wh/kg was obtained at a power density of 160 W/kg which is comparable to or higher than some symmetric and asymmetric supercapacitors such as micro- and meso-porous carbon (<6 Wh/kg),[37] graphene//graphene (~9.1 Wh/kg),[38] CNT//CNT (6 Wh/kg),[39] GH//MnO_2-NF (23.2 Wh/kg),[40] and AC//mesoporous MnO_2 (10.4 Wh/kg).[41] Generally, in supercapacitors, the energy density and power density have an inverse relationship. However, the as-fabricated supercapacitor still showed a high energy density of 11.128 Wh/kg at a power density of 2400 W/kg. The highest energy density and power density achieved for the fabricated ASC are 23.95 Wh/kg and 7200 W/kg, when the potential range used was 0–1.4 V. The various energy and power densities are shown in terms of Ragone plots in Fig. 8a. In order to understand the various resistive parameters involved with the electrochemical phenomenon occurring within the supercapacitor electrodes, EIS analysis was carried out for all three electrode materials along with the fabricated ASC within the frequency range of 50 mHz to 50 kHz. The EIS analysis has been presented in terms of Nyquist plots, shown in Fig. 8b. All the Nyquist plots show a starting semicircle followed by a straight line, characteristic of the charge transfer resistance and Warburg behavior, respectively. The calculated solution resistance (R_s) and the charge transfer resistance (R_{ct}) values of all the prepared electrode materials are tabulated in Table II.

CONCLUSIONS

We have systematically demonstrated the improved energy density and power density of Mn_3O_4@MWCNT//rGO over the Mn_3O_4@MWCNT electrode with proper justification. A synergistic interaction between the highly electrical conductive MWCNT and the pseudocapacitive Mn_3O_4 resulted in higher specific capacitance for the Mn_3O_4@MWCNT//rGO composite compared to that of virgin Mn_3O_4. An aqueous ASC has been constructed which is able to show a high cell voltage of 1.6 V in 1 M KOH electrolyte. The high cell voltage combining the high capacitance of the positive electrode and the high rate capability of the negative electrode results in the high energy density and power density of 26.8 Wh/kg and 2400 W/kg, respectively, for the Mn_3O_4@MWCNT//rGO. The high energy density and power density accompanied by a standard cycle life strongly demonstrate the high efficiency of the as-fabricated supercapacitor for practical purposes.

ELECTRONIC SUPPLEMENTARY MATERIAL

The online version of this article (doi: 10.1007/s11664-016-4493-6) contains supplementary material, which is available to authorized users.

REFERENCES

1. I. Hadjipaschalis, P. Andreas, and E. Venizelos, *Renew. Sustain. Energy Rev.* 13, 1513 (2009).
2. C. Liu, F. Li, L.-P. Maand, and H.-M. Cheng, *Adv. Mater.* 22, E28 (2010).
3. P. Simon and Y. Gogotsi, *Nat. Mater.* 7, 845 (2008).
4. R. Kotz and M. Carlen, *Electrochim. Acta* 45, 2483 (2000).
5. J.W. Long, D. Bélanger, T. Brousse, W. Sugimoto, M.B. Sassin, and O. Crosnier, *MRS Bull.* 36, 513 (2011).
6. Z.-S. Wu, W. Ren, D.-W. Wang, F. Li, B. Liu, and H.-M. Cheng, *ACS Nano* 4, 5835 (2010).
7. J.W. Lee, A.S. Hall, J.D. Kim, and T.E. Mallouk, *Chem. Mater.* 24, 1158 (2012).
8. Y. Xiao, Y. Cao, Y. Gong, A. Zhang, J. Zhao, S. Fang, J. Dianzeng, and F. Li, *J. Power Sources* 246, 926 (2014).
9. X. Du, C. Wang, M. Chen, Y. Jiao, and J. Wang, *J. Phys. Chem. C* 113, 2643 (2009).
10. D. Ghosh, S. Giri, and C.K. Das, *Environ. Prog. Sustain. Energy* 33, 1059 (2014).
11. J. Yan, Z. Fan, W. Sun, G. Ning, T. Wei, Q. Zhang, R. Zhang, L. Zhi, and F. Wei, *Adv. Funct. Mater.* 22, 2632 (2012).

12. D. Ghosh, M. Mandal, and C.K. Das, *Langmuir* 31, 7835 (2015).
13. W. Wei, X. Cui, W. Chen, and D.G. Ivey, *Chem. Soc. Rev.* 40, 1697 (2011).
14. D. Qu, *J. Power Sources* 109, 403 (2002).
15. C. Largeot, C. Portet, J. Chmiola, P.L. Taberna, Y. Gogotsi, and P. Simon, *J. Am. Chem. Soc.* 130, 2730 (2008).
16. M. Mandal, A. Maitra, T. Das, and C.K. Das, *Graphene Materials: Fundamentals and Emerging Applications*, ed. A. Tiwari and M. Syväjärvi (New York: Wiley, 2015), doi: 10.1002/9781119131816.ch1.
17. D.C. Marcano, D.V. Kosynkin, J.M. Berlin, A. Sinitskii, Z. Sun, A. Slesarev, L.B. Alemany, W. Lu, and J.M. Tour, *ACS Nano* 4, 4806 (2010).
18. L. Wang, H. Ji, S. Wang, L. Kong, X. Jiang, and G. Yang, *Nanoscale* 5, 3793 (2013).
19. S. Xiong, C. Yuan, X. Zhang, B. Xi, and Y. Qian, *Chem. Eur. J.* 15, 5320 (2009).
20. L. Wang, H. Ji, F. Zhu, Z. Chen, Y. Yang, X. Jiang, J. Pinto, and G. Yang, *Nanoscale* 5, 7613 (2013).
21. L. Wang, Y. Li, Z. Han, L. Chen, B. Qian, X. Jiang, J. Pinto, and G. Yang, *J. Mater. Chem. A* 1, 8385 (2013).
22. K. Bindumadhavan, S.K. Srivastava, and S. Mahanty, *Chem. Commun.* 49, 1823 (2013).
23. Z.Y. Tian, P.M. Kouotou, N. Bahlawane, and P.H.T. Ngamou, *J. Phys. Chem. C* 117, 6218 (2013).
24. W.Z. Wang, C.K. Xu, G.H. Wang, Y.K. Liu, and C.L. Zheng, *Adv. Mater.* 14, 837 (2002).
25. S.S. Mali, C.A. Betty, P.N. Bhosale, and P.S. Patil, *ECS J. Solid State Sci.* 1, M15 (2012).
26. H. Zhang, D. Hines, and D.L. Akins, *Dalton Trans.* 43, 2670 (2014).
27. T. Yang, L.H. Liu, J.W. Liu, M.L. Chen, and J.H. Wang, *J. Mater. Chem.* 22, 21909 (2012).
28. N. Wu, X. She, D. Yang, X. Wu, F. Su, and Y. Chen, *J. Mater. Chem.* 22, 17254 (2012).
29. L. Malavasi, P. Galinetto, M.C. Mozzati, C.B. Azzoni, and G. Flor, *Phys. Chem. Chem. Phys.* 4, 3876 (2002).
30. L. Li, Z. Guo, A. Du, and H. Liu, *J. Mater. Chem.* 22, 3600 (2012).
31. J.J. Chen, Q. Zhang, Y.N. Shi, L.L. Qin, Y. Cao, M.S. Zheng, and Q.F. Dong, *Phys. Chem. Chem. Phys.* 14, 5376 (2012).
32. F. Chouit, O. Guellati, S. Boukhezar, A. Harat, M. Guerioune, and N. Badi, *Nanoscale Res. Lett.* 9, 1 (2014).
33. H. Estrade-Szwarckopf, *Carbon* 42, 1713 (2004).
34. D.P. Dubal and R. Holze, *New J. Chem.* 37, 403 (2013).
35. C.C. Hu and T.W. Tsou, *Electrochem. Commun.* 4, 105 (2002).
36. T. Zhou, S. Mo, S. Zhou, W. Zou, Y. Liu, and D. Yuan, *J. Mater. Sci.* 46, 3337 (2011).
37. C. Zheng, L. Qi, M. Yoshio, and H. Wang, *J. Power Sources* 195, 4406 (2010).
38. H. Wang, Y. Liang, T. Mirfakhrai, Z. Chen, H.S. Casalongue, and H. Dai, *Nano Res.* 4, 729 (2011).
39. M. Kaempgen, C.K. Chan, J. Ma, Y. Cui, and G. Gruner, *Nano Lett.* 9, 1872 (2009).
40. H. Gao, F. Xiao, C.B. Ching, and H. Duan, *A.C.S. Appl. Mater. Interfaces* 4, 2801 (2012).
41. Y.T. Wang, A.H. Lu, H.L. Zhang, and W.C. Li, *J. Phys. Chem. C* 115, 5413 (2011).